




Cite this: *Mater. Horiz.*, 2017, 4, 681

Received 28th March 2017,  
Accepted 18th May 2017

DOI: 10.1039/c7mh00193b

rsc.li/materials-horizons

## A tale of two membranes: from poly (ionic liquid) to metal–organic framework hybrid nanoporous membranes *via* pseudomorphic replacement†

Jian-Ke Sun,<sup>a</sup> Hui-Juan Lin,<sup>a</sup> Wei-Yi Zhang,<sup>a</sup> Min-Rui Gao,<sup>a</sup> Markus Antonietti<sup>a</sup> and Jiayin Yuan  <sup>\*ab</sup>

**A general approach to produce a variety of free-standing asymmetric MOF hybrid membranes and superstructure arrays on “inert” substrates with tailored crystal sizes and shapes was developed. The obtained MOF hybrid membrane exhibits fast actuation in response to external gas stimulus.**

Metal–organic frameworks (MOFs), as an emerging class of organic–inorganic hybrid porous materials, undergo rapid development owing to the intrinsic characteristic of flexibly designable and controllable skeleton on a molecular scale.<sup>1–5</sup> In comparison to the powdered form of most MOFs reported thus far, MOF-based membranes are structurally exotic and synthetically challenging, but are an evitable step towards device integration for separation, sensing and catalysis applications.<sup>6–8</sup> Current approaches to synthesize the MOF-based membranes include the growth of MOF layers on substrates through surface crystallization,<sup>9–11</sup> interfacial synthesis,<sup>12</sup> layer by layer deposition,<sup>13,14</sup> secondary growth,<sup>15</sup> electrochemical deposition,<sup>16,17</sup> and post-synthetic modification.<sup>18</sup> Very recently, a series of membranes made by incorporation of MOFs into polymer matrices for the purpose of endowing the MOF/polymer hybrid membrane (abbreviated as MOF hybrid membrane hereafter) with benefits from both components has been explored.<sup>19–25</sup> Despite these pioneering studies over the past few years, the compatibility problem between MOF and substrate/matrix and the particle aggregation in MOF-based membranes are still dilemmas.<sup>26–28</sup> Moreover, the control over the crystal size and MOF composition throughout the membrane remains a challenge.<sup>29–32</sup> Therefore, optimizing the existent membrane

### Conceptual insights

Metal–organic frameworks (MOFs) with diverse pore chemistries are currently being actively investigated for membrane fabrication applications. Herein, we present a new concept in the design and synthesis of MOF/polymer hybrid membranes (abbreviated as MOF hybrid membranes hereafter) *via* a templating method. It enables precise spatial control over the nucleation sites of the MOF crystals of tailored sizes and shapes, which form free-standing MOF hybrid membranes and superstructure arrays on “inert” substrates. The success of this approach relies on a morphological replacement procedure that employs a prefabricated ionically crosslinked porous poly (ionic liquid) (PIL) membrane as a reactive template and precursor. The *in situ* transformation from the porous PIL membrane with gradient crosslinking density produces an asymmetric nanoporous MOF hybrid membrane that possesses gradient size and mass distribution of MOF crystals throughout the membrane. The as-synthesized HKUST-1 hybrid membrane, due to its intrinsic asymmetric structure, can actuate at a high speed in contact with NH<sub>3</sub> gas, which is the first example of MOF-based actuators. This work will open new perspectives in the application of MOF membranes for *e.g.* gas sensing/detection. Furthermore, our synthetic concept can be extended to other MOF hybrid membrane systems to reach a high level of structure hierarchy and intriguing functions.

fabrication methods or developing alternative approaches is highly welcomed for further development in this area.

We have recently developed a simple route to fabricate nanoporous poly (ionic liquid) (PIL) membranes *via* ionic cross-linking of a cationic PIL by organic multi-acids (OMAs).<sup>33–35</sup> PILs are an emerging class of functional polymers prepared *via* polymerization of ionic liquids, which demonstrate adjustable solubility in various solvents *via* anion exchange.<sup>36–39</sup> The ability to conveniently create a gradient of crosslinking density across the PIL membrane enables the simultaneous formation of hierarchical nanopores by adjustment of the acid type.<sup>33–35</sup> Ionic bonds featuring a dynamic bonding mode are able to undergo appreciable bonding exchange proportional to ionic strength, so that it can be envisioned that the ionic bond in PIL membranes can be transferred in the presence of certain metal ions into thermodynamically more stable coordination bonds.

<sup>a</sup> Max-Planck-Institute of Colloids and Interfaces, D-14476 Potsdam, Germany.  
E-mail: jiayin.yuan@mpikg.mpg.de

<sup>b</sup> Department of Chemistry & Biomolecular Science & Center for Advanced Materials Processing (CAMP), Clarkson University, 8 Clarkson Avenue, Potsdam, New York 13699, USA. E-mail: jyuan@clarkson.edu

† Electronic supplementary information (ESI) available: Additional characterization of membrane transformation, actuator application and supplementary movie. See DOI: 10.1039/c7mh00193b



If this change stays sufficiently local, the membranes might be transformed into new functional materials *via* a pseudomorphic replacement process. The substantial challenge, therefore, is how to effectively control the growth of new phases on a molecular scale, while maintaining the pores and integrity of the membranes during re-arrangement of ionic bonds.

Herein, we demonstrate a rather general approach to synthesize diverse highly crystalline MOF hybrid membranes through coordination-driven pseudomorphic replacement of porous PIL membranes. The process is reminiscent of pseudomorphic mineral replacement, a natural phenomenon that consists of the transformation of a mineral phase, which is metastable, into a thermodynamically more stable phase.<sup>40–42</sup> One of the impressive features of this process is the high-accuracy preservation of shapes and dimensions of the parent body whenever the degradation of the original phase is slow, compared to the formation of the new phase. The obtained asymmetric MOF hybrid membrane was then applied as an actuator that has a fast response to gaseous stimuli, which inspires futuristic applications of MOF membrane in gas sensing/detection.

Fig. 1 illustrates the synthetic route of MOF hybrid membranes and structure replacement at the molecular level. First, a PIL membrane was synthesized as per ref. 34. Herein, the cationic PIL, poly[3-cyanomethyl-1-vinylimidazolium bis(trifluoromethanesulfonyl)imide] and trimesic acid (denoted as  $H_3BTC$ ) (chemical structures shown in Fig. S1a, ESI<sup>†</sup>) were chosen as the starting materials. The chosen PIL carrying a pendent functional cyano group ( $-C\equiv N$ ) features as coordination sites to effectively anchor the metal sites of the MOF crystals during the transformation process, therefore assisting the binding of the as-formed crystals to the bulk membrane, in addition to the carboxylate in the membrane. The fabrication procedure was started by mixing PIL and  $H_3BTC$  (the imidazolium/COOH molar ratio = 1:1) in a

DMF solution. The formed homogeneous solution was subsequently cast onto a glass plate and dried at 80 °C for 2 h to produce a sticky blend film on the glass plate. It was then immersed in a 0.25 wt% aqueous  $NH_3$  solution for 2 h to induce *in situ* ionic complexation between  $BTC^{3-}$  and the surrounding PIL chains to build up the electrostatically crosslinked porous membrane (pore formation mechanism in Fig. S2, ESI<sup>†</sup>). Note that the side in direct contact with the  $NH_3$  solution is termed as “top surface”, while the other side of the membrane in contact with the glass plate is the “bottom surface”. The as-formed PIL membrane can be easily peeled off from the glass substrate. The resultant membrane contained a gradient profile in both the crosslinking density and the pore size along the cross-section of the membrane (Fig. 1). The pores were the smallest (20–50 nm in size) on the top of the membrane and gradually increased to 0.5–2  $\mu m$  toward the bottom (Fig. 3a–d). The difference in pore size results from the diffusive penetration of ammonia into the polymer film on the glass substrate and is coupled with a gradient of cross-linking density being highest on the top and lowest at the bottom (detailed in Fig. S2, ESI<sup>†</sup>).<sup>34</sup>

In the following pseudomorphic replacement step (Fig. S3, ESI<sup>†</sup>), HKUST-1 ( $Cu_3(BTC)_2$ ) was chosen as a target MOF phase, which is a prototypical porous framework composed of an array of Cu–Cu paddlewheels, connected in three dimension by  $BTC^{3-}$ .<sup>43</sup> The procedure was performed by immersing a free-standing PIL membrane ( $3.5 \times 3\text{ cm}^2$ ) into a 0.1 M  $Cu(NO_3)_2$  solution (6 ml) in a DMF/ethanol/water mixture (volume ratio = 1:2:3). The replacement process was first monitored by UV-vis

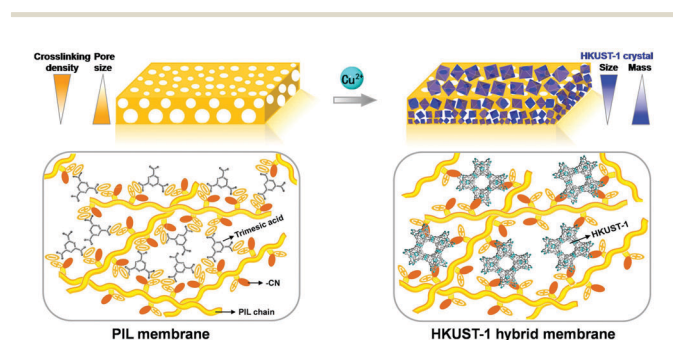


**Fig. 1** A schematic of the pseudomorphic replacement approach to the preparation of an asymmetric MOF (HKUST-1) hybrid membrane (right) from a porous PIL membrane (left) template and precursor. The HKUST-1 hybrid membrane features a gradient structure with increased mass and decreased crystal size from the top to the bottom part of membrane. Bottom left: The yellow line and gray ring represent the PIL polymer chains and  $BTC^{3-}$  molecules, respectively. Bottom right: The open framework represents HKUST-1 built up from  $BTC^{3-}$  and the added metal ions. Fig. 1 schematizes the breaking of the electrostatic ionic complexation by coordination ions and spontaneous formation of the HKUST-1 phase, glued together by the leftover PIL and more locally by the cyano group (red ellipse) of the PIL polymer, which promotes integrity of the macroscopic morphology.

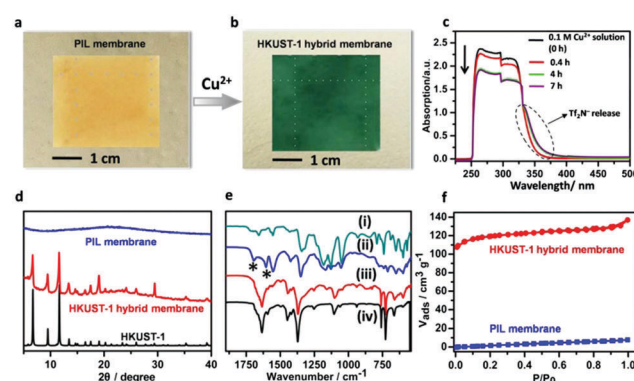


**Fig. 2** Characterization of membrane pseudomorphic replacement process. (a and b) Photographs of PIL membrane and HKUST-1 hybrid membranes. (c) UV-vis spectra of  $Cu(NO_3)_2$  absorption at different time intervals by immersing PIL membrane ( $3.5 \times 3\text{ cm}^2$ ) into 0.1 M  $Cu(NO_3)_2$  solution (6 ml) of DMF/ethanol/water mixture (volume ratio = 1:2:3). No absorption peaks of  $BTC^{3-}$  (Fig. S4, ESI<sup>†</sup>) and PIL (Fig. S5, ESI<sup>†</sup>) were observed, indicating no degradation of the membrane during the replacement process. Variation in the absorption band around 380 nm could be detected due to the  $Tf_2N^-$  (bis(trifluoromethanesulfonyl)imide) anion. (d) XRD patterns of membrane at different synthetic stages. (e) FT-IR spectra of (i) PIL membrane before  $NH_3$ -triggered crosslinking, (ii) PIL membrane after  $NH_3$ -triggered crosslinking in solution. Bands at 1604 and 1698  $cm^{-1}$  (asterisks) are the deprotonated and protonated carboxylate groups, (iii) the obtained HKUST-1 hybrid membrane from the replacement process, (iv) the as-synthesized HKUST-1 powder sample. (f) The  $N_2$  sorption isotherms of HKUST-1 hybrid membrane and PIL membrane.



spectroscopy (Fig. 2c). A decrease in the absorption of  $\text{Cu}(\text{NO}_3)_2$  at 250–330 nm in solution during the immersing time was observed, indicating that  $\text{Cu}(\text{II})$  was extracted from solution into the membrane. This observation was consistent with the color change of the membrane from yellow (Fig. 2a) to green (Fig. 2b). Metal incorporation reached equilibrium after 4 h as its UV-vis spectrum remained constant after that period. It was notable that the membrane maintained its macroscopic integrity during the entire process. The formation of MOF crystals was confirmed by X-ray diffraction (XRD) measurements (Fig. 2d). A clear variation in the XRD pattern from amorphous to crystalline characteristics was observed, the peak positions being consistent with the formation of a HKUST-1 phase. The process was also associated with enhanced Brunauer–Emmett–Teller (BET) specific surface area ( $S_{\text{BET}}$  from 24 to  $362 \text{ m}^2 \text{ g}^{-1}$ ) (Fig. 2f) and the  $\text{CO}_2$  uptake (from 9 to  $60 \text{ cm}^3 \text{ g}^{-1}$ ) due to the formation of the microporous HKUST-1 (Fig. S6, ESI†) in the membrane. The effect of the transformation on the meso- and macroporosity of the membrane was further analyzed by mercury porosimetry (Fig. S7, ESI†). The significant decrease in mercury uptake as well as the pore size indicated that the portion of large meso- and macropores is reduced during the accommodation of the MOF crystals in the membrane pores.

The morphology of the HKUST-1 hybrid membrane was investigated by scanning electron microscopy (SEM) (Fig. 3e–h). The crystalline HKUST-1 particles and the integration within the PIL phase could be clearly observed in the replaced membrane. It was further demonstrated by energy-dispersive X-ray (EDX) mapping of the membrane before and after replacement (Fig. S8, ESI†), where new signals assigned to Cu were visible. Infrared (IR) spectra detected a shift in the vibration band of the carboxylate groups from  $1604 \text{ cm}^{-1}$  and  $1698 \text{ cm}^{-1}$  (deprotonated and protonated carboxylate groups in the PIL membrane, respectively) to  $1635 \text{ cm}^{-1}$ , indicating that all carboxylate groups participated in the coordination with  $\text{Cu}(\text{II})$  to form the HKUST-1 scaffold (Fig. 2e; further evidence detailed in Fig. S10–S12, ESI†). Notably, the gradient in the size of the HKUST-1 crystals from the

membrane top to the bottom can be quantified. As shown in Fig. 3e–h, the HKUST-1 crystals on the top surface of the membrane were 1–2  $\mu\text{m}$  in size, whereas the size dropped to 50–200 nm at the bottom (Fig. S9 (ESI†) with high magnification). Moreover, the EDX analysis of the Cu signal revealed that the membrane also bore a gradient in mass distribution of HKUST-1 along its cross-section (Fig. S10, ESI†) from 10.8 wt% of Cu on the top gradually to 18.9 wt% at the bottom. To the best of our knowledge, such asymmetrical arrangement of MOF crystals throughout the membrane in a size and mass gradient has not been reported previously.

The *in situ* accurate replacement process at a molecular scale is responsible for such unprecedented precision. Given the asymmetric mass distribution of  $\text{BTC}^{3-}$  (both free and complexed forms) in the porous PIL membrane, *i.e.* more  $\text{BTC}^{3-}/\text{H}_3\text{BTC}$  at the bottom than the top region (see ESI† Fig. S11 and S12), it is reasonable for the resultant HKUST crystals in the hybrid membrane to follow the same mass gradient distribution. As for the size gradient, whether the carboxylate in  $\text{BTC}^{3-}$  is in a free or a complexed form matters. The gradient in the crosslinking density is also referred to as a gradient in the density of complexed carboxylate groups (thus also the free carboxylate groups) of  $\text{BTC}^{3-}$  in the parent PIL membrane. In the crystallization of the MOFs, large crystals form when nucleation is slow, relative to crystal growth.<sup>44,45</sup> In our study, the nucleation principally occurs as long as free carboxylate groups are exposed to the metal containing solution, and crystal growth stops when all accessible carboxylate groups, after being gradually released from the crosslinks, are depleted. In the PIL membrane, the carboxylate groups in the upper part are highly crosslinked with PIL, *i.e.*, less free carboxylate groups are available for immediate coordination with  $\text{Cu}(\text{II})$ , which in turn makes nucleation with  $\text{Cu}(\text{II})$  kinetically slower in comparison to that at the membrane bottom. In short, higher cross-linking density suppresses nucleation rate, and such crystals grow larger. Reasonably, such a process leads to disparity in crystallization rates across the membrane due to different kinetics in bond rearrangements, resulting in asymmetric size distribution of the HKUST-1 crystals.

It is surprising that no macroscopic degradation of the membrane on the millimeter and centimeter scales was observed in the replacement process, highlighting the advantage of our approach toward MOF hybrid membrane fabrication. We speculated that this is supported by the pendant cyano group on PIL, which can also bind to the  $\text{Cu}(\text{II})$  site at the surface of the HKUST-1 crystal during the transformation process, *i.e.*, membrane replacement and membrane stabilization occurs simultaneously. In fact, one can observe the immediate precipitation after mixing a PIL solution with a  $\text{Cu}(\text{II})$  solution, indicative of strong interaction between the two. X-ray photoelectron spectroscopy (XPS) measurement of the precipitate confirmed the coordination between the cyano group in the PIL and  $\text{Cu}(\text{II})$  (Fig. S13, ESI†). In addition, we observed a ligand-to-metal charge-transfer (LMCT) transition due to the coordination between the cyano group and  $\text{Cu}(\text{II})$  in the final HKUST-1 hybrid membrane (Fig. S14b, ESI†). To further cross-prove the important role of the cyano functionality in the PIL in

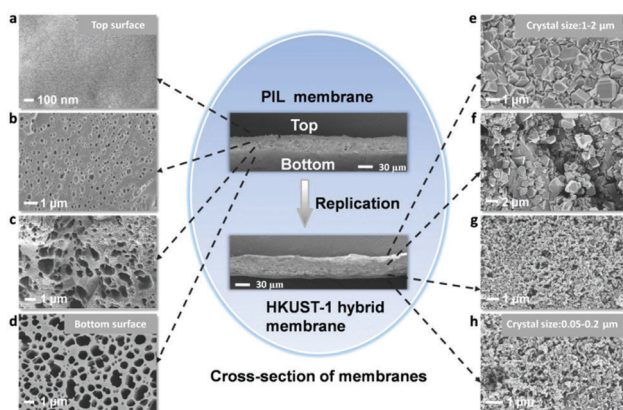


Fig. 3 The SEM images recorded at different positions of the PIL membrane and HKUST-1 hybrid membrane. PIL membrane: (a) top surface; (b) upper part; (c) lower part; (d) bottom surface. HKUST-1 hybrid membrane: (e) top surface; (f) upper part; (g) lower part; (h) bottom surface, and the high magnification of bottom surface is shown in Fig. S9 (ESI†).





maintaining the integrity of the membrane in the replacement process, a control experiment using a similar membrane with an ethyl-containing PIL (chemical structure in Fig. S1b, ESI†) as a template and precursor (denoted as PIL-ethyl) was carried out. Notably, disruption of this membrane was observed right after its immersion in the same concentration of Cu(II) solution, along with the formation of small, green cracks determined to be a HKUST-1 phase by XRD (Fig. S15, ESI†). This indicates that the coordination between Cu(II) and BTC<sup>3-</sup> induced the decomposition of the PIL-ethyl membrane without sufficient binding strength of the re-liberated PIL to the crystals. In fact, we did not observe strong interaction between the PIL-ethyl membrane and Cu(II) as no precipitation occurred on mixing their solutions. These experiments demonstrate the crucial function of the cyano group as a binder and membrane morphology “stabilizer” during the replacement process. It is notable that the existence of a macroporous structure is a prerequisite for the replacement. If a nonporous PIL membrane is used, the transfer to the HKUST-1 phase would be incomplete since the lack of pore structure would severely slow down or even block metal ion diffusion of all the carboxylate groups into the membrane (Fig. S16, ESI†). Furthermore, the macropores accommodate a part of the crystals and minimize the internal strain that otherwise may fracture the membrane. It should be mentioned that the obtained HKUST-1 hybrid membrane is stable in aggressive solvents (e.g., DMF) as well as in atmospheric environments (relative humidity: 20~30%) over two months, as confirmed by XRD measurements (Fig. S17 and S18, ESI†).

The present replacement approach is robust for large-scale synthesis of HKUST-1 hybrid membranes, which herein is exemplified with a piece of 13 × 22 cm<sup>2</sup> in size (see TOC). Moreover, it is also applicable for other asymmetric MOF hybrid membranes such as MOF-74-Co and Cu-BDC, by employing PIL, and the corresponding acids, H<sub>4</sub>DOBDC (2,5-dihydroxyterephthalic acid) and H<sub>2</sub>BDC (1,4-benzenedicarboxylic acid), respectively. The successful replacements were demonstrated by XRD as well as SEM measurements (Fig. S19–S22, ESI†).

In addition to the fabrication of free-standing MOF hybrid membranes, the present concept could be extended to the growth and positioning of MOF arrays on a variety of “inert” substrates to obtain free-standing MOF superstructures. It is well-known that the direct growth of MOF crystals on “inert” substrates is a challenge due to the poor compatibility between highly crystalline MOFs and bare substrates without any further surface functionalization.<sup>26–28,46</sup> Therefore, control of heterophase nucleation on such types of substrates is a difficult task. Over the past few years, PILs have been recognized as surface-active polymers that can serve as “universal coating” agents to modify surfaces ranging from metals and metal oxides to carbon atoms.<sup>33,35,47–49</sup> In other words, they are able to form homogeneous and robust coatings or layers on all common surfaces optimized by the choice of the backbone, anion and cation in their chemical structures to achieve multiple interactions<sup>50</sup> (such as Coulomb interaction, cation- $\pi$  interaction, van der Waals' force or other charge polarized interactions) with the substrate. Such intriguing properties can guide the growth

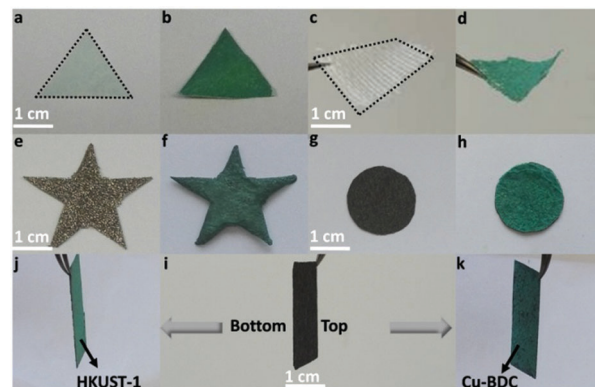


Fig. 4 Schematic of the growth of MOF arrays on various “inert” substrates for obtaining MOF superstructures with controlled shapes. Photographic images of (a) filter paper in a triangle form (highlighted edge by a dotted line). (b) HKUST-1@filter paper. (c) Cotton textile in a rectangular form (highlighted edge by a dotted line). (d) HKUST-1@cotton textile. (e), Nickel foam in a star form. (f) HKUST-1@nickel foam. (g) Carbon paper. (h) HKUST-1@carbon paper. The growth of Janus MOF hybrid membrane with HKUST-1 (j) and Cu-BDC (k) on each side of the carbon paper (i).

of MOFs essentially on universal substrates. Herein, several representative substrates (e.g., filter paper, carbon paper, nickel foam and cotton textile) with different components, shapes and hardness/softness were chosen for the growth of HKUST-1 (Fig. 4). The typical procedure involves the fabrication of a thin porous PIL membrane on these substrates, followed by immersion of the PIL membrane@substrate into the Cu(II) solution (Fig. S23a, ESI†). The successful growth of a uniform HKUST-1 coating was confirmed by XRD and SEM measurements (Fig. S23–S26, ESI†). The mechanical robustness of these MOF structures is one of the critical prerequisites in practical applications. Abrasion resistance tests were performed through adhesion with adhesive tape. HKUST-1 growth on nickel foam through the PIL interface could maintain its structure and morphology and possessed better performance in comparison to HKUST-1 growing on the bare nickel foam substrate (Fig. S27, ESI†). Notably, we could also realize the asymmetric Janus MOF hybrid membrane by growing HKUST-1 and Cu-BDC on each side of the carbon paper (Fig. 4j, k and Fig. S28, ESI†). The Janus structure combined with the PIL assisted replacement method significantly broadens the diversity of multifunctional MOF hybrid membranes for a wide range of applications.

The asymmetric MOF hybrid membranes are associated with new functions and applications. Herein, we discovered that a free-standing HKUST-1 hybrid membrane could be used as an actuator in response to NH<sub>3</sub> gas stimulus, which has not been recognized in MOF based membranes to date. When HKUST-1 hybrid membrane was moved from air to NH<sub>3</sub> gas ( $T = 20\text{ }^{\circ}\text{C}$ , 857 kPa), the flat membrane (11 mm × 2 mm × 38  $\mu\text{m}$ ) bent quickly into a hemi-loop in  $\sim 0.5\text{ s}$  with the top surface inwards (Fig. 5 and Movie 1, ESI†). Upon annealing in air at 80  $^{\circ}\text{C}$ , the membrane recovered its original shape (Fig. 5 and Movie 2, ESI†). The actuation process can be repeated (4 cycles in Fig. S29, ESI†), though a slight decrease in the curvature occurs due to the high affinity of NH<sub>3</sub> gas to HKUST-1.



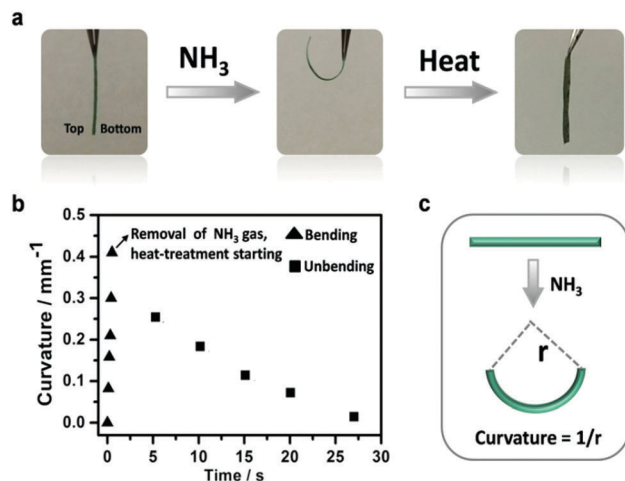


Fig. 5 Application of HKUST-1 hybrid membrane actuator toward  $\text{NH}_3$  response. (a) Adaptive movement of a HKUST-1 hybrid membrane ( $11 \text{ mm} \times 2 \text{ mm} \times 38 \mu\text{m}$ ) placed in  $\text{NH}_3$  gas and then back after heat treatment. (b) Plot of curvature against time for the membrane actuator in (a). (c) A scheme of how the curvature is calculated.

The kinetics of the bending and unbending movements is assessed by plotting the curvature of the membrane against time (Fig. 5b), resulting in a bending curvature of  $0.42 \text{ mm}^{-1}$  in  $0.5 \text{ s}$ . Since the curvature of bending scales inversely with membrane thickness,<sup>35</sup> we plotted 'curvature  $\times$  thickness' versus time, with the purpose to compare the actuation speed of the present membrane actuator with previously reported prototypical soft actuators in the literature (summarized in supporting references). As shown in Fig. 6, the present actuation speed is well beyond many conventional prototypical soft actuators, such as polymer membranes, liquid crystals and other soft materials (Table S1, ESI†).

Generally speaking, a polymer or its hybrid membrane bends when asymmetric swelling strains are generated across the membrane in contact with trigger molecules.<sup>51–54</sup> In the

present case, the native PIL membrane interacts only weakly with  $\text{NH}_3$  gas (Fig. S30, ESI†), while HKUST-1 is known to bind with  $\text{NH}_3$  via coordination with the  $\text{Cu}(\text{II})$  site (Fig. S31, ESI†),<sup>55–58</sup> and expands in volume after the uptake of the guests, which was reported previously<sup>59,60</sup> and observed experimentally by us (Fig. S32, ESI†). The HKUST-1 crystals, in terms of size and relative contribution, are asymmetrically distributed in the membrane, i.e. small HKUST-1 crystals are at the bottom and large ones on the top (Fig. 3). In addition, as discussed previously, the absolute mass of the HKUST-1 crystals at the bottom is the highest and decreases gradually to the top (Fig. S10, ESI†). When XPS measurements of the top and bottom sides of the HKUST-1 hybrid membrane were carried out before and after exposure to  $\text{NH}_3$  gas, a shift ( $\Delta$ ) in the binding energy of  $\text{Cu } 2\text{P}$  to a lower position upon  $\text{NH}_3$  absorption could be detected in both sides (Fig. S33 and S34, ESI†), which was larger at the bottom ( $\Delta = 0.5$  and  $0.7 \text{ eV}$  for  $\text{Cu } 2\text{P}_{3/2}$  and  $\text{Cu } 2\text{P}_{1/2}$ , respectively) than on the top ( $\Delta = 0.1$  and  $0.1 \text{ eV}$  for  $\text{Cu } 2\text{P}_{3/2}$  and  $\text{Cu } 2\text{P}_{1/2}$ , respectively). This observation unambiguously indicates that the interaction between  $\text{NH}_3$  and the HKUST-1 crystals is stronger at the bottom (nanometer-sized crystals) than on the top (micrometer-sized crystals) of the membrane. This is presumably due to the accelerated and full gas penetration in nanometer-sized crystals<sup>61</sup> and less hindered shape changes. The synergistic action of higher mass and higher relative binding results in higher swelling of the membrane at the bottom, creating bending with the top layer inwards (Fig. S35, ESI†). Previous studies have demonstrated that even a small difference in strain (generated by gradient chemical reaction, physical sorption, swelling etc.) can drive the bending actuation.<sup>62–66</sup> This statement is in good agreement with our observation that little-to-no variation in morphology and phase of the membrane actuator was detected upon the bending/unbending process (Fig. S36 and S37, ESI†). Heating the bent membrane could partially release incorporated  $\text{NH}_3$  molecules (evidenced by IR spectra in Fig. S31, ESI†) and reverse it to its flat state. To evidence the function of the gradient structural profile, we prepared a control HKUST-1 hybrid membrane by mixing pre-synthesized HKUST-1 crystals with the PIL and then casting their dispersion on a glass substrate. The SEM image showed random distribution of HKUST-1 crystals across the membrane (Fig. S38, ESI†) and no actuation of the membrane towards  $\text{NH}_3$  gas (Fig. S39, ESI†).

It is noteworthy that the actuation speed in the MOF hybrid membrane is very fast compared to other prototypical soft actuators (Table S1, ESI†). This kinetic advantage could stem from the combined pore design, i.e. the microporous HKUST-1 crystals in a macroporous polymer matrix, which accelerates transport of  $\text{NH}_3$  gas diffusion. In fact, the present membrane could serve as an  $\text{NH}_3$  gas sensor as Fig. S40 (ESI†) quantitatively showed that the curvature of the actuator is linearly proportional to  $\text{NH}_3$  gas content. Considering the advantage of the ordered microporous structures, particularly their ability to modulate adsorbate species, the development of asymmetric MOF hybrid membranes with task-specific sensing application in terms of visual actuation is foreseeable.

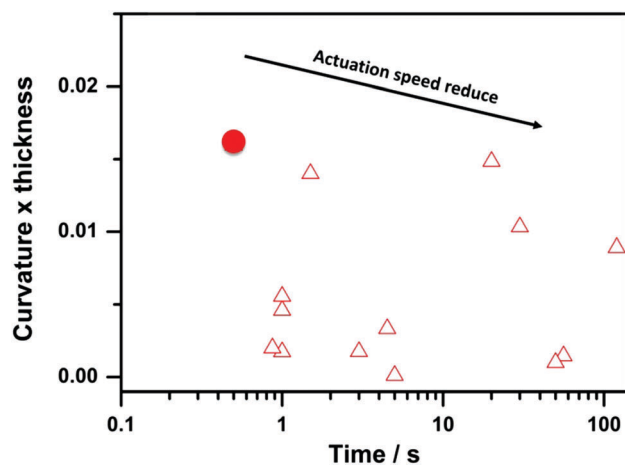


Fig. 6 Plot of 'curvature  $\times$  thickness' against time for the membrane actuator in the current work (red solid circle) and prototypical soft actuators from pervious literature (Table S1, ESI†) results (red empty triangle). The faster actuators are found in the top left of this diagram.

In conclusion, we described a robust coordination replacement protocol that allows the access of asymmetric MOF hybrid membranes. The kinetics and spatial coupling between the removal of ionic bonds and the immediate formation of coordination bonds enable the production of MOF hybrid membranes with well-grown and dispersed crystals through a pseudomorphic replacement. Assisted by the gradient of the porous PIL membrane as both reactive template and precursor, highly crystalline MOF crystals with controlled sizes and mass distribution can be located and arranged throughout the membrane precisely. The as-synthesized MOF hybrid membrane with asymmetric and microporous structure exhibits several useful but also some unexpected properties, illustrated here by fast actuation in response to  $\text{NH}_3$  stimulus. We believe that our concept of MOF hybrid membrane synthesis will inspire custom design of further MOF-based membranes with a high level of structure hierarchy and complexity.

## Acknowledgements

This study was supported by the Max Planck Society. J. Y. thanks the European Research Council Starting Grant (639720-NAPOLI). J. K. S thanks AvH (Alexander von Humboldt) foundation for a postdoctoral fellowship. Open Access funding provided by the Max Planck Society.

## Notes and references

- H. Li, M. Eddaoudi, M. O'Keeffe and O. M. Yaghi, *Nature*, 1999, **402**, 276–279.
- G. Férey, *Chem. Soc. Rev.*, 2008, **37**, 191–214.
- S. T. Meek, J. A. Greathouse and M. D. Allendorf, *Adv. Mater.*, 2011, **23**, 249–267.
- J. R. Li, J. Yu, W. Lu, L. B. Sun, J. Sculley and H. C. Zhou, *Nat. Commun.*, 2013, **4**, 1538.
- S. Xiang, Y. He, Z. Zhang, H. Wu, W. Zhou, R. Krishna and B. Chen, *Nat. Commun.*, 2012, **3**, 954.
- M. Shah, M. C. McCarthy, S. Sachdeva, A. K. Lee and H. K. Jeong, *Ind. Eng. Chem. Res.*, 2012, **51**, 2179–2199.
- S. Qiu, M. Xue and G. Zhu, *Chem. Soc. Rev.*, 2014, **43**, 6116–6140.
- B. Seoane, J. Coronas, I. Gascon, M. E. Benavides, O. Karvan, J. Caro, F. Kapteijn and J. Gascon, *Chem. Soc. Rev.*, 2015, **44**, 2421–2454.
- A. Huang, W. Dou and J. Caro, *J. Am. Chem. Soc.*, 2010, **132**, 15562–15564.
- E. Biemmi, C. Scherb and T. Bein, *J. Am. Chem. Soc.*, 2007, **129**, 8054–8055.
- C. R. Wade, M. Li and M. Dincă, *Angew. Chem., Int. Ed.*, 2013, **52**, 13377–13381.
- A. J. Brown, N. A. Brunelli, K. Eum, F. Rashidi, J. R. Johnson, W. J. Koros, C. W. Jones and S. Nair, *Science*, 2014, **345**, 72–75.
- O. Shekhah, H. Wang, S. Kowarik, F. Schreiber, M. Paulus, M. Tolan, C. Sternemann, F. Evers, D. Zacher, R. A. Fischer and C. Wöll, *J. Am. Chem. Soc.*, 2007, **129**, 15118–15119.
- S. Sakaida, K. Otsubo, O. Sakata, C. Song, A. Fujiwara, M. Takata and H. Kitagawa, *Nat. Chem.*, 2016, **8**, 377–383.
- F. Zhang, X. Zou, X. Gao, S. Fan, F. Sun, H. Ren and G. Zhu, *Adv. Funct. Mater.*, 2012, **22**, 3583–3590.
- R. Ameloot, L. Stappers, J. Fransaer, L. Alaerts, B. F. Sels and D. E. De Vos, *Chem. Mater.*, 2009, **21**, 2580–2582.
- M. Li and M. Dincă, *Chem. Sci.*, 2014, **5**, 107–111.
- Y. Liu, J. H. Pan, N. Wang, F. Steinbach, X. Liu and J. Caro, *Angew. Chem., Int. Ed.*, 2015, **54**, 3028–3032.
- S. Basu, M. Maes, A. Cano-Odena, L. Alaerts, D. E. De Vos and I. F. J. Vankelecom, *J. Membr. Sci.*, 2009, **344**, 190–198.
- M. J. C. Ordoñez, K. Balkus Jr, J. J. P. Ferraris and I. H. Musselman, *J. Membr. Sci.*, 2010, **361**, 28–37.
- T. H. Bae and J. R. Long, *Energy Environ. Sci.*, 2013, **6**, 3565–3569.
- M. S. Denny, Jr. and S. M. Cohen, *Angew. Chem., Int. Ed.*, 2015, **54**, 9029–9032.
- Y. Zhang, X. Feng, H. Li, Y. Chen, J. Zhao, S. Wang, L. Wang and B. Wang, *Angew. Chem., Int. Ed.*, 2015, **54**, 4259–4263.
- T. Rodenas, I. Luz, G. Prieto, B. Seoane, H. Miro, A. Corma, F. Kapteijn, F. X. L. Xamena and J. Gascon, *Nat. Mater.*, 2015, **14**, 48–55.
- P. Zhang, H. Li, G. M. Veith and S. Dai, *Adv. Mater.*, 2015, **27**, 234–239.
- R. Zhang, S. Ji, N. Wang, L. Wang, G. Zhang and J. R. Li, *Angew. Chem., Int. Ed.*, 2014, **53**, 9775–9779.
- Y. Liu, N. Wang, J. H. Pan, F. Steinbach and J. Caro, *J. Am. Chem. Soc.*, 2014, **136**, 14353–14356.
- R. Semino, N. A. Ramsahye, A. Ghoufi and G. Maurin, *ACS Appl. Mater. Interfaces*, 2016, **218**, 809–819.
- T. T. Y. Tan, M. R. Reithofer, E. Y. Chen, A. G. Menon, T. S. Andy Hor, J. Xu and J. M. Chin, *J. Am. Chem. Soc.*, 2013, **135**, 16272–16275.
- W. Li, Y. Zhang, C. Zhang, Q. Meng, Z. Xu, P. Su, Q. Li, C. Shen, Z. Fan, L. Qin and G. Zhang, *Nat. Commun.*, 2016, **7**, 11315.
- A. Sabetghadam, B. Seoane, D. Keskin, N. Duim, T. Rodenas, S. Shahid, S. Sorribas, C. Le Guillouzer, G. Clet, C. Tellez, M. Daturi, J. Coronas, F. Kapteijn and J. Gascon, *Adv. Funct. Mater.*, 2016, **26**, 3154–3163.
- P. Falcaro, K. Okada, T. Hara, K. Ikigaki, Y. Tokudome, A. W. Thornton, A. J. Hill, T. Williams, C. Doonan and M. Takahashi, *Nat. Mater.*, 2017, **16**, 342–348.
- Q. Zhao, P. Zhang, M. Antonietti and J. Yuan, *J. Am. Chem. Soc.*, 2012, **134**, 11852–11855.
- K. Täuber, Q. Zhao, M. Antonietti and J. Yuan, *ACS Macro Lett.*, 2014, **4**, 39–42.
- Q. Zhao, J. W. C. Dunlop, X. Qiu, F. Huang, Z. Zhang, J. Heyda, J. Dzubiella, M. Antonietti and J. Yuan, *Nat. Commun.*, 2014, **5**, 4293.
- H. He, M. Zhong, B. Adzima, D. Luebke, H. Nulwala and K. Matyjaszewski, *J. Am. Chem. Soc.*, 2013, **135**, 4227–4230.
- X. Sui, M. A. Hempenius and G. J. Vancso, *J. Am. Chem. Soc.*, 2012, **134**, 4023–4025.
- J. K. Sun, M. Antonietti and J. Yuan, *Chem. Soc. Rev.*, 2016, **45**, 6627–6656.



- 39 P. Zhang, M. Li, B. Yang, Y. Fang, X. Jiang, G. M. Veith, X. G. Sun and S. Dai, *Adv. Mater.*, 2015, **27**, 8088–8094.
- 40 A. Putnis, *Rev. Mineral. Geochem.*, 2009, **70**, 87–124.
- 41 Y. Jiang, H. Gong, M. Grzywa, D. Volkmer, L. Gower and H. Cölfen, *Adv. Funct. Mater.*, 2012, **23**, 1547–1555.
- 42 J. Reboul, S. Furukawa, N. Horike, M. Tsotsalas, K. Hirai, H. Uehara, M. Kondo, N. Louvain, O. Sakata and S. Kitagawa, *Nat. Mater.*, 2012, **11**, 717–723.
- 43 S. S. Y. Chui, S. M. F. Lo, J. P. H. Charmant, A. G. Orpen and I. D. Williams, *Science*, 1999, **283**, 1148–1150.
- 44 S. Diring, S. Furukawa, Y. Takashima, T. Tsuruoka and S. Kitagawa, *Chem. Mater.*, 2010, **22**, 4531–4538.
- 45 S. M. Meckler, C. Li, W. L. Queen, T. E. Williams, J. R. Long, R. Buonsanti, D. J. Milliron and B. A. Helms, *Chem. Mater.*, 2015, **27**, 7673–7679.
- 46 X. Yang, X. Jiang, Y. Huang, Z. Guo and L. Shao, *ACS Appl. Mater. Interfaces*, 2017, **9**, 5590–5599.
- 47 P. Zhang, J. Yuan, T. P. Feller, M. Antonietti, H. Li and Y. Wang, *Angew. Chem., Int. Ed.*, 2013, **52**, 6028–6032.
- 48 T. P. Feller, A. Thomas, J. Yuan and M. Antonietti, *Adv. Mater.*, 2013, **25**, 5838–5855.
- 49 C. Willa, J. Yuan, M. Niederberger and D. Koziej, *Adv. Funct. Mater.*, 2015, **25**, 2537–2542.
- 50 J. Yuan, M. Drechsler, Y. Xu, M. Zhang and A. H. E. Muller, *Polymer*, 2008, **49**, 1547–1554.
- 51 J. Liang, L. Huang, N. Li, Y. Huang, Y. Wu, S. Fang, J. Oh, M. Kozlov, Y. Ma, F. Li, R. Baughman and Y. Chen, *ACS Nano*, 2012, **6**, 4508–4519.
- 52 W. E. Lee, Y. J. Jin, L. S. Park and G. Kwak, *Adv. Mater.*, 2012, **24**, 5604–5609.
- 53 O. Kim, T. J. Shin and M. J. Park, *Nat. Commun.*, 2013, **4**, 2208.
- 54 J. Deng, J. Li, P. Chen, X. Fang, X. Sun, Y. Jiang, W. Weng, B. Wang and H. Peng, *J. Am. Chem. Soc.*, 2016, **138**, 225–230.
- 55 D. Britt, D. Tranchemontagne and O. M. Yaghi, *Proc. Natl. Acad. Sci. U. S. A.*, 2008, **105**, 11623–11627.
- 56 B. Supronowicz, A. Mavrandonakis and T. Heine, *J. Phys. Chem. C*, 2013, **117**, 14570–14578.
- 57 J. B. DeCoste, M. S. Denny, Jr., G. W. Peterson, J. J. Mahle and S. M. Cohen, *Chem. Sci.*, 2016, **7**, 2711–2716.
- 58 D. Wiser, F. M. Wiser, S. Raschke, N. Klein, M. Leistner, J. Grothe, E. Brunner and S. Kaskel, *Angew. Chem., Int. Ed.*, 2015, **54**, 12588–12591.
- 59 T. Baimpos, B. R. Shrestha, Q. Hu, G. Genchev and M. Valtiner, *J. Phys. Chem. C*, 2015, **119**, 16769–16776.
- 60 M. D. Allendorf, R. J. T. Houk, L. Andruszkiewicz, A. A. Talin, J. Pikarsky, A. Choudhury, K. A. Gall and P. J. Hesketh, *J. Am. Chem. Soc.*, 2008, **130**, 14404–14405.
- 61 D. Tanaka, A. Henke, K. Albrecht, M. Moeller, K. Nakagawa, S. Kitagawa and J. Groll, *Nat. Chem.*, 2010, **2**, 410–416.
- 62 S. Kobatake, S. Takami, H. Muto, T. Ishikawa and M. Irie, *Nature*, 2007, **446**, 778–781.
- 63 J. K. Sun, W. Li, C. Chen, C. X. Ren, D. M. Pan and J. Zhang, *Angew. Chem., Int. Ed.*, 2013, **52**, 6653–6657.
- 64 T. Lan and W. Chen, *Angew. Chem., Int. Ed.*, 2013, **52**, 6496–6500.
- 65 K. Iwasa, Y. Takashima and A. Harada, *Nat. Chem.*, 2016, **8**, 625–632.
- 66 H. Arazoe, D. Miyajima, K. Akaike, F. Araoka, E. Sato, T. Hikima, M. Kawamoto and T. Aida, *Nat. Mater.*, 2016, **15**, 1084–1089.

